Astronomy & Astrophysics manuscript no. CKVul_paper_shock
February 4, 2022

Elemental abundances in the remnant of the ancient eruption of CK Vulpeculae

R. Tylenda[1], T. Kamiński[2⋆], A. Mehner[3],

[1] Nicolaus Copernicus Astronomical Center, Polish Academy of Sciences, Rabiańska 8, 87-100 Toruń, e-mail: tylenda@ncac.torun.pl
[2] Center for Astrophysics, Harvard & Smithsonian, 60 Garden Street, Cambridge, MA, USA, e-mail: tkaminsk@cfa.harvard.edu
[3] ESO, Alonso de Cordoba 3107, Vitacura, Santiago, Chile, e-mail: amehner@eso.org

February 4, 2022

ABSTRACT

CK Vul or Nova 1670 is an enigmatic eruptive object which underwent a stellar-merger event recorded by seventeenth-century observers. Its remnant was recently recovered at submillimeter wavelengths, revealing gas of an extraordinary isotopic composition indicative of past processing in the CNO cycles and partial He burning. Here, we present long-slit optical spectra of the remnant acquired with X-shooter at the Very Large Telescope at an unprecedented sensitivity and spectral coverage. The spectra cover features of key elements – including H, He, C, N, and O – at ionization degrees I–III. A classical analysis of the spectra allows us to identify several spatio-kinematic components in the probed part of the nebula at electron temperatures of 10–15 kK and densities of 200–600 cm^{-3}. We find that the nebula is most likely excited by shocks rather than by direct radiation of the stellar remnant. We provide a detailed analysis of the elemental abundances in the remnant and find that helium is twice more abundant than in the Sun. Nitrogen is also overabundant with a N/O ratio ten times larger than the solar one. These anomalous abundances strongly indicate that the observed gas was processed in CNO cycles of H burning, consistent with the submillimeter studies. Additionally, sub-solar abundances of heavier elements, such as Ne, S, and Ar, suggest that the progenitor of CK Vul was formed from material poorer in metals than the Sun and was therefore an old stellar system before the 1670 eruption.

1. Introduction

CK Vulpeculae (CK Vul) is a remnant of a naked-eye stellar eruption observed in 1670–72 (Hevelius 1671; Shara et al. 1985). For a long time it was considered a classical nova (that is, a thermonuclear explosion on an accreting white dwarf), despite its unusual light curve that displayed three peaks over a time span of nearly three years. The stellar remnant is not seen in the optical but a faint hourglass nebula is visible around the presumable position of the 1670 nova (Shara & Moffat 1982; Shara et al. 1985; Hajduk et al. 2007). The stellar object is however relatively bright in the far infrared (Evans et al. 2002; Kamiński et al. 2015a). This implies that the stellar remnant is obscured by an opaque dusty envelope whose sole presence is yet another argument against the classical nova scenario. Provoked by the enigma, Kamiński et al. (2015a) launched a pioneering spectroscopic study of CK Vul at submillimeter (submm) wavelengths using the APEX telescope and the Submillimeter Array (SMA). The observations revealed that it is a strong and rich source of molecular emission. Kamiński et al. concluded that the 1670 eruption was that of a *red nova* rather than a classical nova – a hypothesis already discussed in the past (Kato 2003; Tylenda et al. 2013).

It was the 2002 eruption of V838 Monocerotis (e.g., Munari et al. 2002) which raised a wide interest and allowed astrophysicists to define a new class of stellar eruptions named red novae or red transients. An increasingly red color implying a decreasing effective temperature is the primary characteristic of red novae. After the eruption, lasting a month up to a few years in the optical, the transients decline as very late M-type supergiants although they remain bright in the infrared for decades (or longer). Following a discussion of different mechanisms responsible for red-nova eruptions, Soker & Tylenda (2003) and next Tylenda & Soker (2006) proposed a binary merger as the scenario that best explains the observations of red novae. A 2008 eruption of V1309 Scorpii (Mason et al. 2010) was crucial for solving the red nova enigma. Using archival photometry of the object secured by the OGLE project (Udalski 2003) and available for six years prior to the 2008 eruption, Tylenda et al. (2011) showed that before the eruption V1309 Scorpii was a contact binary with a rapidly decreasing orbital period.

Submillimeter spectroscopy revealed a very rich molecular enviroment of CK Vul's remant (Kamiński et al. 2015a, 2017). Kamiński et al. (2017) identified over 320 unique spectral features belonging to 27 molecules and their isotopologues. It has since been established that molecular emission at submm wavelengths is a common feature of Galactic red-nova remnants (Kamiński et al. 2018a). The great advantage of measuring rotational molecular lines at submm wavelengths is that they allow to determine the isotopic composition of the observed molecular matter. Kamiński et al. (2017) derived isotopic ratios of five elements in CK Vul: C, N, O, Si, and S. The isotopes of C, N, and O are of a particular importance as their isotopic ratios can reveal what nuclear burning processes occurred in the progenitor and, perhaps, during the merger. Kamiński et al. concluded that the gas currently seen in the remnant was processed in the CNO cycles of H-burning and underwent partial He burning.

Recently, very sensitive spectroscopy of CK Vul, acquired with mm-wave interferometers ALMA and NOEMA, led to a discovery of the rare isotopologue of aluminum fluoride that contains the radioactive isotope of aluminum, ^{26}AlF (Kamiński et al. 2018b). This was the first astronomical observation of a radioactive isotopologue in a stellar object, demonstrating once again the extraordinary properties of the CK Vul remnant. The observation yields a very low $^{27}\mathrm{Al}/^{26}\mathrm{Al}$ ratio of about 7 which

⋆ Submillimeter Array Fellow

indicates that the gas in the remnant had to be recently processed in the hot Mg–Al cycles of H-burning. Most probably, the unstable isotope of Al comes from the outer layers of a He-core of a red giant disrupted in the merger that was witnessed in 1670–72. Eyres et al. (2018) questioned this interpretation and, based on a current low luminosity (1–10 $L_{\odot}$) and potential overabundance of Li in the remnant (Hajduk et al. 2013), proposed instead that Nova 1670 was a merger of a white dwarf and a brown dwarf.

Unfortunately, the submm spectroscopy alone cannot provide us with a quntitative measure of elemental abundances, which would be very useful for constraining the nature of the CK Vul's progenitor. Judging from a particularly high strength of lines of N-bearing molecules, Kamiński et al. (2017) suggested however that nitrogen is overabundant in the remnant (see also Shara et al. 1985); similarly, the C/O ratio could be close to or slightly above one (see also Evans et al. 2016).

The optical nebula of CK Vul offers a possibility of deriving stringent constraints on the elemental abundances in the remnant. The abundances can be derived from nebular line intensities using well-established analysis methods commonly applied to planetary nebulae, H II regions, and active galactic nuclei (e.g. Osterbrock & Ferland 2006). However, the nebular regions of CK Vul are very weak and spectra of CK Vul obtained thus far (Shara et al. 1985; Hajduk et al. 2007, 2013) are of modest quality so that only a few strongest lines have been measured. This has hampered any advanced study of elemental abundances in this peculiar object. Here we present (Sects. 2–3) and analyze (Sects. 3–4) an optical spectrum of CK Vul nebula obtained at an unprecedented sensitivity. With this spectrum, we are able to derive the elemental abundances for the brightest part of the CK Vul nebula (Sect. 5) and discuss their origin (Sect. 6).

2. Observations

CK Vul was observed with X-shooter (Vernet et al. 2011) at the Very Large Telescope (VLT) on 29 Jul, and 15, 17, 18, and 27 Aug 2017. X-shooter records spectra simultaneously in three spectroscopic arms: UVB (300–560 nm), VIS (550–1020 nm), and NIR (1020–2480 nm). The atmospheric dispersion corrector (ADC) was correcting the observations for the differential atmospheric refraction. This correction is particularly relevant for our observations as they took place at airmass 1.6–1.8. The visual seeing had a full-width at half-maximum (FWHM) of 0.″7–1.″3. The slit has a length of 11″. We set slit widths to 1.″3 for the UVB arm and to 1.″2 for the VIS and NIR arms. This resulted in spectral resolutions, $\lambda/\Delta\lambda$, of 4100, 6500, 4300 in the UVB, VIS, and NIR arms, respectively. The *stare* observing mode was used to increase the observing efficiency for the UVB and VIS arms but it compromised the quality of the NIR part of the spectra. With the large extent of the nebula of CK Vul of 71″ (Hajduk et al. 2013), it would be very difficult to find a nearby nodding position resulting in optimal sky extraction along the entire slit and therefore *stare* mode was a reasonable choice. The UVB and VIS detectors were used in their slow-readout mode with high gain and 1×2 binning. The exposure times per observing block were 3030 and 3060 s for UVB and VIS arms, respectively, adding to about 6 h of on-source observations. Telluric standards, Hip095400, Hip095340, Hip090637, Hip107734, Hip101716, and Hip098609, and spectrophotometric standards, Feige 110 and EG 274, were observed with the same instrumental setup.

The observations were intended to secure a deep spectrum along the brightest part of the optical nebula. The nebula itself is too faint for direct pointing of the telescope. For this reason, the observations were executed with the so-called *blind-offset* procedure in which the demanded position of the slit is given with respect to a brighter field star. This field source is first used for fine positioning of the telescope after which the telescope is slewed to the main target with the implemented offsets. The resulting slit positions are overlaid in Fig. 1 on an average X-shooter acquisition image in the *R*-band filter and on the Gemini/GMOS image from Hajduk et al. (2013) in the Hα filter from 2010. Point sources were subtracted in the latter image to enhance the nebular emission. X-shooter acquisition images are taken immediately before each spectroscopic exposure. We corrected the images for bias and flat-field and combined them with *swarp* (Bertin et al. 2002). We oriented the slit at a position angle (PA) of 13.°0 which is aligned with the northern jet of the atomic emission (cf. Kamiński et al. 2015a). The southern edge of the slit partially overlaps with two background stars. The brighter one Hajduk et al. (2013) recognized as a variable source (their "variable 1"). The slit is close but does not overlap with the expected location of the stellar remnant of CK Vul. The predicted location of the star CK Vul, marked with a cross in Fig. 1, is based on observations of its submm continuum (Kamiński et al. 2018b). The full extent of the slit corresponds to distances of 1.″4–8.″5 to North-East and 1.″4–3.″0 to South-West from that position.

The spectroscopic data were processed with the ESO X-shooter pipeline (Modigliani et al. 2010) version v3.1.0 with standard procedures resulting in two-dimensional spectra calibrated in wavelength and flux. The wavelength calibration has typical uncertainties of about 0.02, 0.03 nm in VIS and UVB spectra, respectively. Background sky correction turned out to be a very sensitive aspect of the data reduction because the nebula and field stars fill almost fully the slit and the off-source sky signal could not be adequately sampled. This problem particularly affected the removal of airglow emission lines. The VIS data were further corrected for telluric absorption with Molecfit version 1.4.0 (Kausch et al. 2015; Smette et al. 2015) using the telluric standards. This correction was imperfect, as well, and left residuals in the regions of the strongest telluric absorption. The wavelength scale of all spectra was then shifted to the heliocentric rest frame and spectra were combined. Some obvious instrumental artifacts were blanked in the spectra by hand. The two-dimensional spectra have a typical rms noise of 1.6×10^{-19} erg cm^{-2} s^{-1} Å^{-1} and the highest recorded signal-to-noise is of 665 at the default pipeline pixel binning of 0.2 Å×0.″16.

3. The spectrum and its spatial characteristics

Figure 2 presents a global spectrum obtained by summing the flux over the entire extent of the source along the slit. The upper panel shows the UBV spectrum while the middle and bottom panels present the VIS spectrum. We omit the spectrum between 740 and 850 nm as it lacks any spectral features. The identification of the most relevant features is shown with red markers. The identified lines are also listed in Tables 1–3. Note that at wavelengths longer than about 870 nm the spectrum is often contaminated by residua of the imperfect telluric correction (see Sect. 2). Over 40 spectral features belonging to eleven elements (H, He, C, N, O, Ne, S, Ar, Fe, Ni, and Ca) at three ionization states (I–III) were identified. The presence of some lines, such as the *D* doublet of Na I, is doubtful owing to interstellar contamination.

Most lines typically observed in planetary nebulae can be found in the spectrum of CK Vul. However, lines of neutral species – i.e., [O I], [N I], and [C I] – are significantly stronger

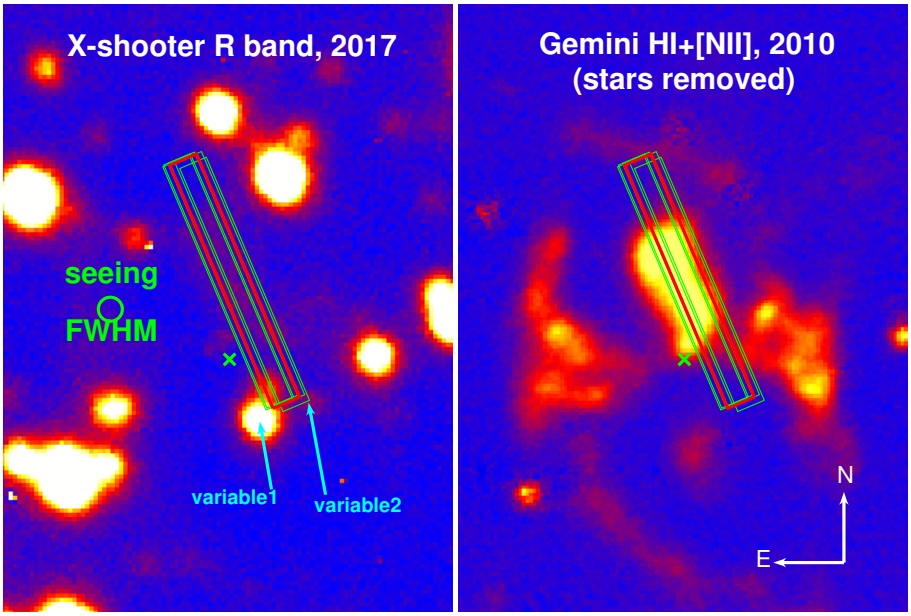

Fig. 1. Slit positions of X-shooter. The slit is represented by a box of a size of 11″×1.″2 and at PA=13°. Positions corresponding to individual exposures are shown with green thin lines and their average position is shown with the red thick line. The background images are all in scale and coaligned. Left: the average X-shooter acquisition image in *R* band. Right: the image of the nebula in the Hα filter from Hajduk et al. (2013) with most point sources removed.

in CK Vul than in a typical planetary nebula (e.g. Górny 2014). Also, emission of singly ionized metals – i.e., [Fe II], [Ni II], and [Ca II] – which are absent in the spectra of planetary nebulae, can easily be identified in Fig. 2. These differences may signify that the excitation mechanism of the CK Vul's nebular emission is different from that in planetary nebulae, i.e. is different than direct ionization by the radiation of the central star. We return to this point in Sect. 6.1.

The quality of our spectrum warrants reliable estimates of the physical conditions in the probed part of the nebula, including the electron temperature, T_e, and electron density, N_e. The fluxes of lines [O III] 438.3, [N II] 575.5, and [S III] 631.2,[1] which are necessary to determine T_e, can be reliably measured. Even the [C I] 872.7 transition, although very weak, can be measured in one kinematical component, enabling another estimate of T_e. The electron density can be derived from the line ratios of [O II] 372.6/372.9, [S II] 671.6/673.1, and [N I] 519.8/520.0. The lines of [O II] and [N I] are partially blended in our spectrum but are sufficiently well resolved to derive their ratios. Having determined T_e and N_e, one can derive the ion abundances and then estimate the abundances of individual elements. For details of the nebular spectrum analysis, see e.g. Chapter 4 and 5 in Osterbrock & Ferland (2006).

Profiles of the emission lines in CK Vul show a complex kinematical sub-structure, distinct for different species and ionization levels. This is illustrated in Fig. 3 which shows two-dimensional distributions of emission in Hβ, [O III] 500.7, and [N II] 658.3 along the slit as a function of velocity (or wavelength). The emission covers a wide range of radial velocities, generally from ∼–350 to ∼+300 km s^{-1}, but the velocity range depends on the line and the position along the slit. The main emission concentrates in two 'wings' forming a structure with a shape of the letter 'V' (Fig. 3). Hereafter, we refer to the left (negative-velocity) 'wing' as component A and the right one as component B. At a velocity of about –300 km s^{-1} and a position –2.″5 along the slit, there is also a weaker emission feature which we identify as component C. The three components are roughly indicated in the bottom right panel of Fig. 3.

[1] All lines in this paper are identified by their laboratory air wavelength in nm.

As can be seen in Fig. 3, the emission in Hβ comes from all three components. This is obviously also the case for the other identified H I lines. Emission of He I is observed in components A and B but is almost absent in component C. Instead, the [N II] emission is concentrated in components A and C. This is also true for all lines of singly ionized and neutral species, i.e. [O I], [O II], [N I], [S II], etc. Component B dominates the emission in the [O III] lines and the lines from other doubly ionized species ([Ne III], [S III], and [Ar III]). The components readily differ in excitation conditions. Specifically, the excitation of plasma in component B is significantly higher than in components A and C.

Because of these excitation differences, we did not analyze the global spectrum presented in Fig. 2, but rather disentangled the spectra of individual spatio-kinematic components and analyzed them separately. However, A and B are partially blended and the degree of blending depends on the range of pixels chosen for summing along the slit. After several attempts to optimize this separation, we took three spatial cuts shown in the bottom right panel of Fig. 3 with dashed lines. *Spectrum 1* was obtained by summing emission in pixels located within a region between l=–0.″64 to 0.″30 with respect to the slit center (with negative values representing the direction towards South-West). This central spectrum extraction includes the maximum emission of the strongest lines. *Spectrum 2* was extracted by adding fluxes for 1.″75≤ l ≤4.″14. In this spectrum, components A and B are better separable than in *spectrum 1* but the line emission is weaker, especially in component B. A third spectrum was produced by summing the flux in –2.″60≤ l ≤–2.″25, meant to study component C.

4. Line intensities and extinction

Figure 4 displays typical line profiles in spectrum 1, representing the central extraction. The Hβ emission displays two clear peaks corresponding to components A and B. The [O III] line shows a single component arising from region B. Contrary to this, the [N II] line arises mainly in component A.

As is best seen in the Hβ profile in Fig. 4, the emission of components A and B is partially blended. We disentangled them by fitting two Gaussian profiles to the observed features. The

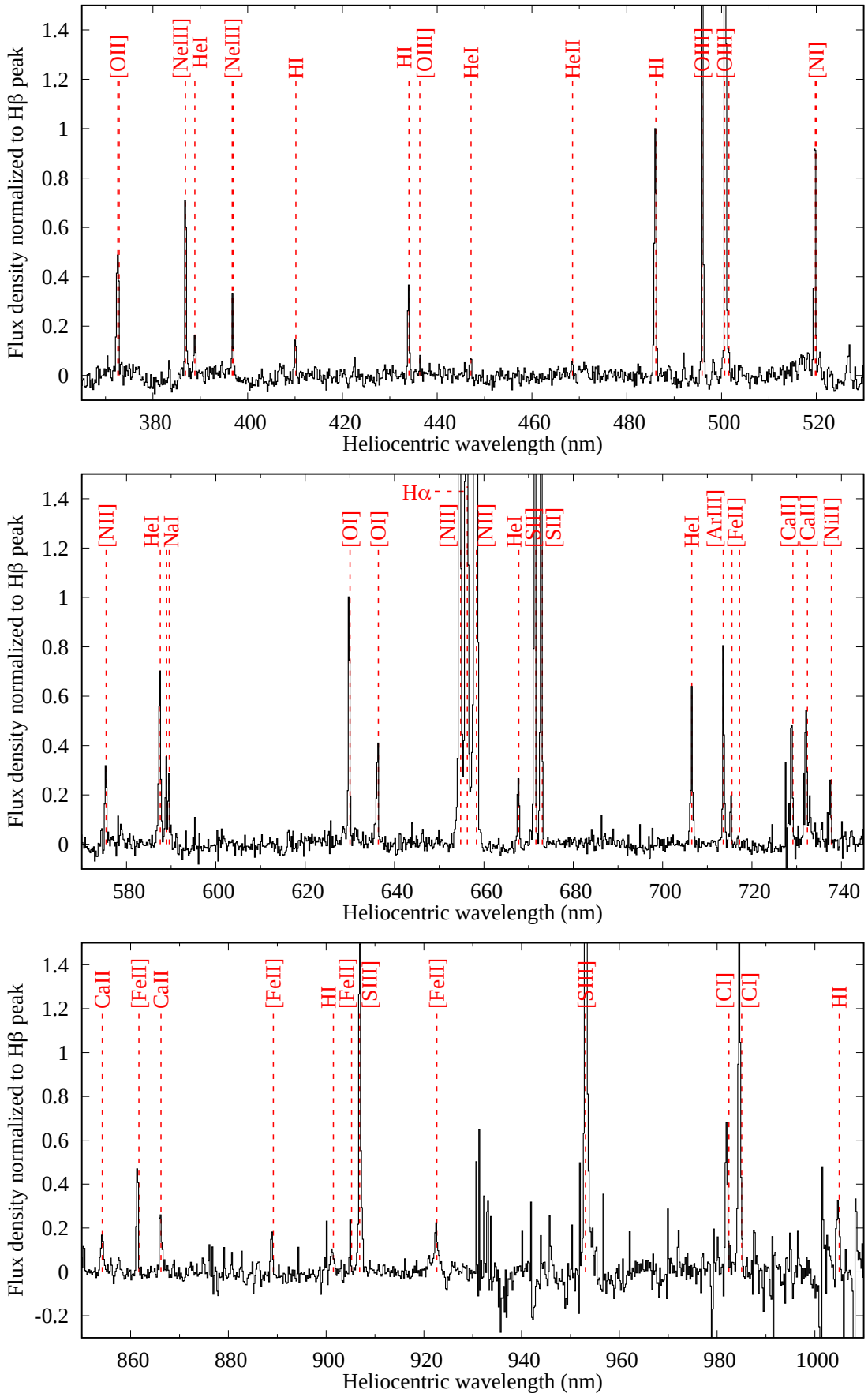

Fig. 2. Spectrum of the brightest nebular region of CK Vul obtained with X-shooter. The spectrum was obtained by summing the flux over the entire slit and smothing the spectral axis with 10 pixel average. Our identification of the major emission lines is shown in red. The vertical markers are drawn at rest laboratory wavelengths.

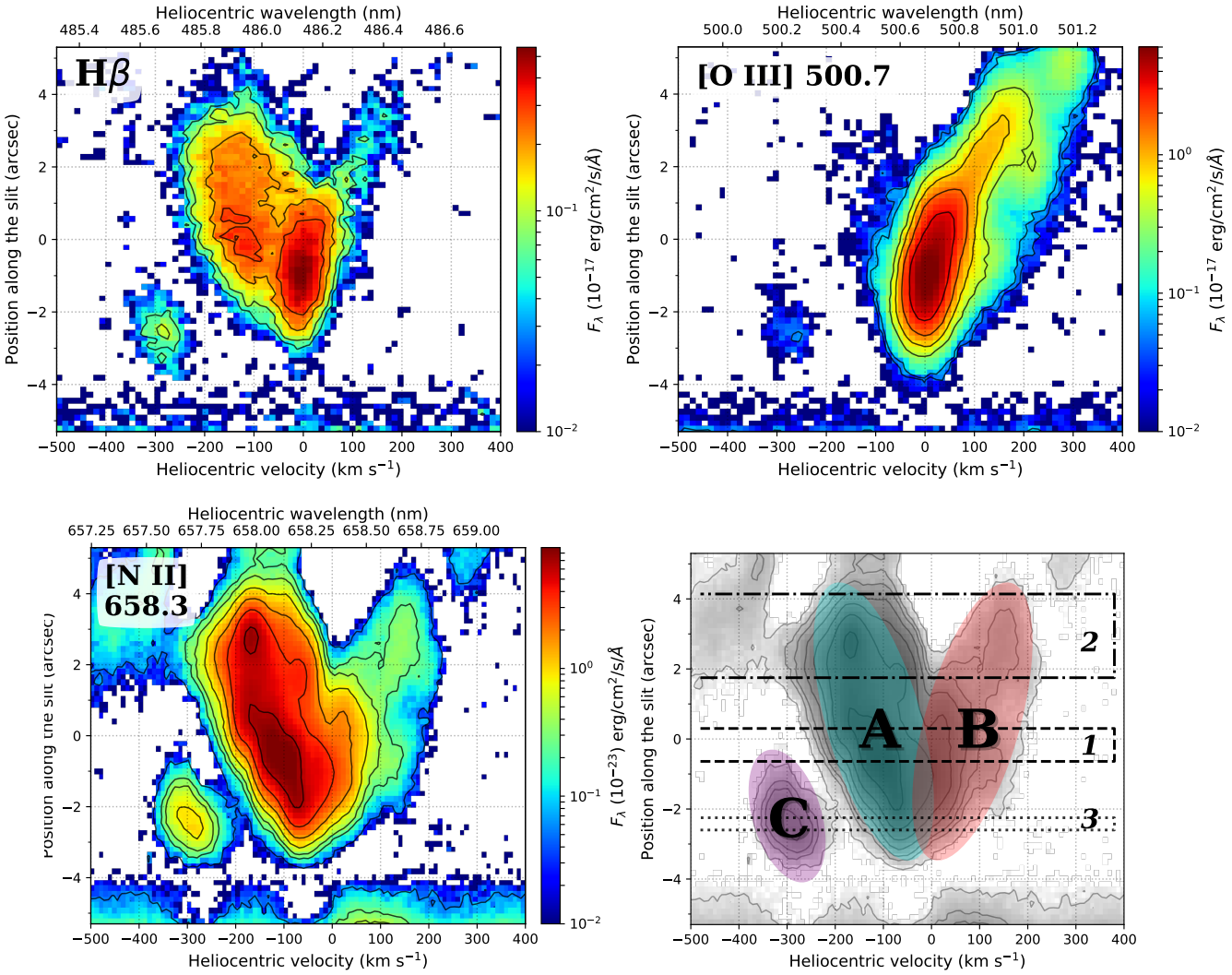

Fig. 3. Sample two-dimensional spectra of emission along the slit. Three emission lines are shown: Hβ with contours at [3, 5, 10, 15]$\times\sigma$ noise levels; [O III] 500.7 with countours at [3, 5, 25, 50, 100, 200]$\times\sigma$; and [N II] 658.3 with contours at [3, 15, 25, 50, 100, 200, 400]$\times\sigma$. The lower right panel is the same map of [N II] (grey color scale) where we roughly deliminated with color shaded areas regions A, B, and C defined in the text. The dashed lines indicate the location of the three extracted spectra discussed in the text.

individual Gaussian profiles are plotted with dotted curves and their sum is shown with a dashed curve. We adopted the integral over the fitted Gaussian as the flux of the corresponding component. To have consistent measurements, the procedure of fitting a Gaussian profile was also applied to lines showing a single component, e.g to the [O III] line in Fig. 4.

The results of the Gaussian fits to the emission line profiles of spectrum 1 are presented in Table 1. They include measurements of the flux (within the defined extraction aperture which was different for the three spectra), relative flux (scaled so that Hβ has a value of 100), central radial velocity (V_r), FWHM, and an estimate of flux uncertainties (column headed "Note").

The radial velocity of component A in spectrum 1, calculated as the mean radial velocity of lines with good Gaussian fits, is $\langle V_r\rangle$=–116 km s^{-1}. The mean FWHM, calculated in the same way is $\langle\theta\rangle$=112 km s^{-1}. This value includes the instrumental broadening. FWHM of the instrumental profile, as estimated from airglow lines, is $\simeq$ 35 km s^{-1}. Thus, FWHM of component A in spectrum 1 corrected for instrumental broadening is $\langle\theta_c\rangle$=106 km s^{-1}. The same figures for component B are 13 km s^{-1} and 100 km s^{-1} ($\langle\theta_c\rangle$=94 km s^{-1}), respectively.

Figure 5 is analogues to Fig. 4 and displays line profiles and Gaussian fits for spectrum 2 extracted in the East-North part of the slit. In this region, components A and B are easier to separate than in spectrum 1. Component B is much weaker than component A. The profile of [N II] 658.3 in component A is not well reproduced by the Gaussian. It is narrower and shifted to more negative velocities than the profile of Hβ. Readily, component A has a somewhat more complex structure in spectrum 2 than in 1. The derived line parameters are summarized in Table 2. The meaning of the columns is the same as in Table 1.

In spectrum 2, the mean radial velocity and the mean FWHM for component A are $\langle V_r\rangle$=–141 km s^{-1} and $\langle\theta\rangle$=136 km s^{-1} ($\langle\theta_c\rangle$=131 km s^{-1}), while for component B these figures are $\langle V_r\rangle$=143 km s^{-1} and $\langle\theta\rangle$=132 km s^{-1} ($\langle\theta_c\rangle$=127 km s^{-1}). The separation of the components in spectrum 2 is greater than in spectrum 1 and the line profiles in spectrum 1 are somewhat wider. The latter is partially due to the larger range of pixels included in extraction of spectrum 2 compared to spectrum 1.

Spectrum 3 was obtained solely to study component C (see Fig. 3). There is a component produced by blending A and B in this spectrum but it is well separated from C and does not affect

Table 1. Measurements of emission lines in spectrum 1.

λ_0 (nm)	Ion	component A Flux (10^{-16} erg cm^{-2} s^{-1})	Relative flux (Hβ=100)	V_r (km s^{-1})	FWHM (km s^{-1})	Note	component B Flux (10^{-16} erg cm^{-2} s^{-1})	Relative flux (Hβ=100)	V_r (km s^{-1})	FWHM (km s^{-1})	Note
372.60	[O II]	0.200	50.0	–90	132	a					
372.88	[O II]	0.184	46.0	–100	120	a					
386.88	[Ne III]						0.574	118.6	16	89	a
388.86	He I	0.057	14.3	–108	94	c	0.069	14.3	24	113	c
396.75	[Ne III]						0.145	30.0	18	94	a
397.01	H I	0.022	5.5	–120	130	c	0.027	5.6	10	101	c
410.17	H I	0.056	14.0	–120	144	b	0.064	13.2	10	101	b
434.05	H I	0.131	32.8	–120	118	b	0.152	31.4	10	99	b
436.32	[O III]						0.054	11.2	17	78	b
447.15	He I	0.028	7.0	–102	104	c	0.042	8.7	11	87	c
468.57	He II	0.024	6.0	–118	89	c	0.030	6.2	22	92	c
486.13	H I	0.400	100.0	–120	118	a	0.484	100.0	10	101	a
495.89	[O III]						1.632	337.2	19	87	a
500.68	[O III]						5.064	1046.3	20	87	a
501.57	He I	0.034	8.5	–107	101	c	0.046	9.5	11	92	c
519.79	[N I]	0.280	70.0	–123	118	b					
520.03	[N I]	0.340	85.0	–125	120	b					
575.46	[N II]	0.123	30.8	–103	106	b	0.160	33.1	9	89	b
587.56	He I	0.250	62.5	–129	97	a	0.403	83.3	8	106	a
630.03	[O I]	0.480	120.0	–116	101	b					
631.21	[S III]						0.060	12.4	17	87	b
636.38	[O I]	0.175	43.8	–118	115	b					
654.80	[N II]	4.296	1074.0	–114	106	a	1.288	266.1	2	120	b
656.28	H I	3.240	810.0	–138	92	a	4.000	826.4	–2	118	a
658.34	[N II]	13.500	3375.0	–114	108	a	3.920	809.9	2	120	b
667.82	He I	0.116	29.0	–123	101	b	0.145	30.0	12	94	b
671.64	[S II]	1.648	412.0	–125	97	a					
673.08	[S II]	1.600	400.0	–125	97	a					
706.52	He I	0.082	20.5	–136	80	b	0.413	85.3	17	101	a
713.58	[Ar III]						0.547	113.0	13	99	a
715.52	[Fe II]	0.145	36.3	–104	108	b					
717.20	[Fe II]	0.024	6.0	–113	108	c					
729.15	[Ca II]	0.419	104.8	–112	141	b					
732.39	[Ca II]	0.445	111.3	–123	146	b					
737.78	[Ni II]	0.205	51.3	–103	115	b					
745.26	[Fe II]	0.052	13.0	–102	92	c					
861.70	[Fe II]	0.461	115.3	–103	115	b					
901.49	H I	0.048	12.0	–138	80	c	0.052	10.7	–2	118	c
905.20	[Fe II]	0.138	34.5	–100	92	b					
906.86	[S III]	0.075	18.8	–110	54	c	1.280	264.5	25	115	a
922.66	[Fe II]	0.110	27.5	–95	141	b					
922.90	H I	0.067	16.8	–135	82	c	0.083	17.1	22	134	c
953.06	[S III]	0.196	49.0	–110	54	b	3.620	747.9	25	115	a
954.60	H I	0.079	19.8	–134	80	c	0.096	19.8	–6	82	c
982.41	[C I]	0.372	93.0	–128	141	b					
985.03	[C I]	0.946	236.5	–130	127	a					
1004.98	H I	0.183	45.8	–147	99	c	0.225	46.5	–14	122	c

Notes. The first two columns identify the lines including their laboratory wavelength, λ_0. The five subsequent columns present results of Gaussian fits to component A and the last five columns to component B. The fluxes are given in absolute units and relative to Hβ (×100). They represent the same region along the spatial axis for regions A and B but different than that used in Tables 2 and 3. V_r is the central radial velocity of the line derived in the fit. Last column quantifies the flux measurements: a, flux accurate to within 10%; b, error between 10 and 30%; c, error greater than 30%.

our fits. The measurements are presented in Table 3. The mean radial velocity of component C is $\langle V_r \rangle$=–285 km s^{-1}, while the mean FWHM of the lines is $\langle \theta \rangle$=84 km s^{-1}($\langle \theta_c \rangle$=76 km s^{-1}).

The spectra are heavily reddened. We corrected the spectra for reddening using the extinction curve of Draine (2003).[2] To evaluate the amount of extinction, we followed the standard procedure often applied to nebular spectra and matched the observed Balmer decrements to the theoretical one (cf. Table 4.4 in Osterbrock & Ferland 2006). A particular attention was given to reproduce the right ratio of Hα to Hβ as it is most sensitive to the value of extinction. Other Balmer lines are rather faint in the observed spectrum so their measured fluxes are subject to larger errors. Table 4 presents the extinction-corrected fluxes normalized to Hβ and multiplied by 100. The first row names the spectra (e.g. A1 stands for component A in spectrum 1). The second

[2] available at www.astro.princeton.edu/~draine/dust/dust.html

Table 2. The same as Table 1 but for spectrum 2.

λ_0 (nm)	Ion	component A Flux (10^{-16} erg cm^{-2} s^{-1})	Relative flux (Hβ=100)	V_r (km s^{-1})	FWHM (km s^{-1})	Note	component B Flux (10^{-16} erg cm^{-2} s^{-1})	Relative flux (Hβ=100)	V_r (km s^{-1})	FWHM (km s^{-1})	Note
372.60	[O II]	0.320	37.1	–124	167	a					
372.88	[O II]	0.326	37.8	–124	167	a					
386.88	[Ne III]	0.063	7.3	–126	203	c	0.358	214.4	140	148	a
388.86	He I	0.109	12.6	–119	134	b	0.044	26.3	118	120	c
396.75	[Ne III]	0.021	2.4	–126	188	d	0.105	62.9	124	92	b
410.17	H I	0.131	15.2	–118	177	b	0.015	9.0	137	118	d
434.05	H I	0.292	33.9	–122	179	b	0.053	31.7	137	118	b
436.32	[O III]						0.020	12.0	145	148	d
447.15	He I	0.075	8.7	–125	193	c					
486.13	H I	0.862	100.0	–129	177	a	0.167	100.0	137	115	a
495.89	[O III]	0.023	2.7	–127	106	d	0.960	574.9	144	153	a
500.68	[O III]	0.069	8.0	–127	106	c	2.960	1772.5	142	151	a
519.79	[N I]	0.800	92.8	–146	94	a					
520.03	[N I]	0.869	100.8	–146	94	a					
575.46	[N II]	0.188	21.8	–137	127	c					
587.56	He I	0.543	63.0	–147	160	a	0.176	105.4	141	137	b
630.03	[O I]	0.937	108.7	–157	92	a					
636.38	[O I]	0.338	39.2	–159	99	b					
654.80	[N II]	6.752	783.3	–151	127	a	0.716	428.7	134	139	b
656.28	H I	7.240	839.9	–149	146	a	1.352	809.6	136	134	a
658.34	[N II]	21.500	2494.2	–151	130	a	1.512	905.4	134	139	a
667.82	He I	0.250	29.0	–128	177	b	0.072	43.1	107	174	c
671.64	[S II]	3.526	409.0	–153	104	a					
673.08	[S II]	3.276	380.0	–154	104	a					
706.52	He I	0.187	21.7	–160	134	b	0.197	118.0	154	141	b
713.58	[Ar III]						0.247	147.9	145	127	a
715.52	[Fe II]	0.159	18.4	–134	151	b					
729.15	[Ca II]	0.640	74.2	–140	137	b					
732.39	[Ca II]	0.442	51.3	–141	148	b					
737.78	[Ni II]	0.203	23.5	–132	139	b					
861.70	[Fe II]	0.530	61.5	–138	148	b					
872.71	[C I]	0.080	9.3	–160	106	c					
889.19	[Fe II]	0.227	26.3	–134	165	b					
901.49	H I	0.113	13.1	–136	118	c					
906.86	[S III]	0.100	11.6	–161	179	d	0.473	283.2	164	111	a
922.66	[Fe II]	0.074	8.6	–160	94	c					
922.90	H I	0.143	16.6	–129	80	c					
953.06	[S III]	0.328	38.1	–161	179	c	1.568	938.9	166	144	a
982.41	[C I]	1.344	155.9	–161	104	b					
985.03	[C I]	3.816	442.7	–157	97	a					

Notes. The first two columns identify the lines including their laboratory wavelength, λ_0. The five subsequent columns present results of Gaussian fits to component A and the last five columns to component B. The fluxes are given in absolute units and relative to Hβ (×100). They represent the same region along the spatial axis for regions A and B but different than that used in Tables 1 and 3. V_r is the central radial velocity of the line. Last column quantifies the flux measurements: a, flux accurate to within 10%; b, error between 10 and 30%; c, error greater than 30%; d, line marginally detected.

row gives the adopted value of the logarithmic extinction, C, at Hβ and the corresponding value of E_{B-V} in the third row.

5. Derivation of T_e, N_e, and abundances

Determination of the elemental abundances in CK Vul is the primary goal of the present study. The theory of line emission processes in nebular conditions is well understood (e.g. Ch. 4 and 5 in Osterbrock & Ferland 2006). There are two kinds of line-excitation mechanisms relevant for ionized nebulae. The lines of H I, He I, and He II are emitted mainly due to recombination of the H and He ions. The lines of heavier elements, mostly forbidden ones, are produced by collisional excitation of the lowest levels of neutral atoms and ions with free electrons.

We performed the analysis of collisionally excited (forbidden) lines in CK Vul by solving the statistical-equilibrium equation for a given electron temperature and density and in a five-level model of a given ion (atom).[3] The necessary radiative prob-

[3] As we argue later on in this paper, the matter in the investigated nebular region of CK Vul can be out of the ionization and thermal equilibria. One may think that in that case the assumption of statistical equilibrium is not satisfied as well, affecting the ionic level populations. However, the processes governing the level populations are much faster than those governing the ionization state. In our case ($N_e \simeq 500\,\mathrm{cm}^{-3}$ and $T_e \simeq 10^4$ K), the collisional excitation and de-excitation of low-lying levels of atoms and ions proceeds on a time scale of hours, while the recombination of ionized hydrogen takes hundreds of years. The physical conditions (N_e and T_e) in the nebular region of CK Vul certainly do not vary on a time scale of hours or days (this region has been observed for

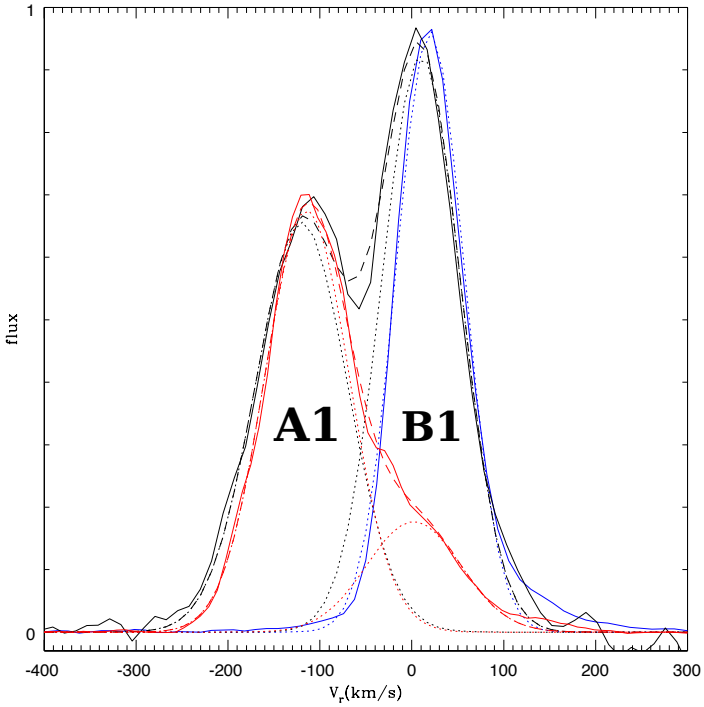

Fig. 4. Emission line profiles in spectrum 1. Full curves represent observed profiles of Hβ (black), [N II] 658.3 (red), and [O III] 500.7 (blue). Dotted curves show Gaussian components fitted to the observed profiles. The dashed curve is the sum of the Gaussian components.

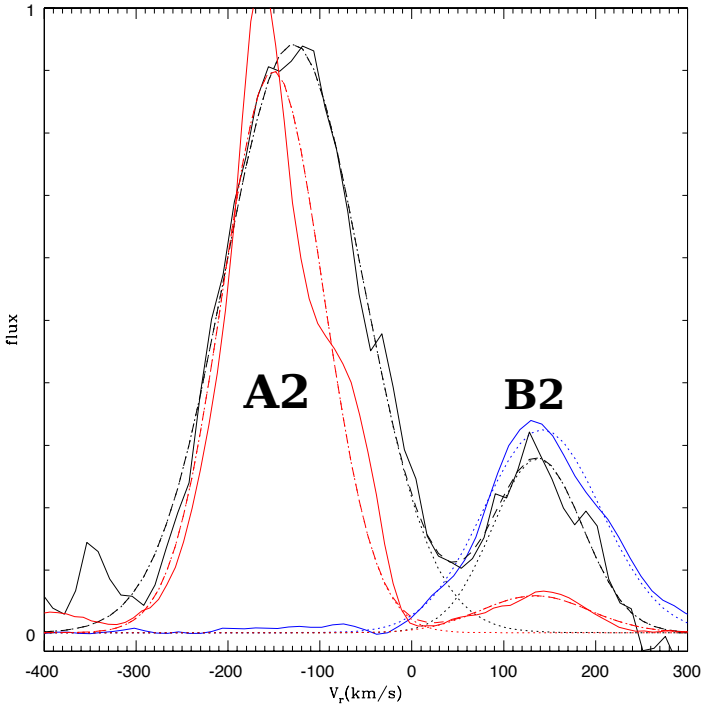

Fig. 5. The same as Fig. 4 but for spectrum 2.

abilities and effective collision strengths were taken from a compilation[4] of Pradhan & Peng (1995).

The electron temperature, T_e, was derived by adjusting the model $(^1S - ^1D)/(^1D - ^3P)$ line ratio to the observed values of [C I], [N II], [O III], and [S III]. The same was performed for the $(^2D_{3/2} - ^4S)/(^2D_{5/2} - ^4S)$ line ratio of [N I], [O II], and [S II] which yields estimates of the electron density, N_e.

The results are given in Table 5. The first part of the table gives our estimates of T_e. They rely on the quality of the $(^1S - ^1D)$ lines, which are often faint in our spectra. Hence the accuracy of the T_e determinations, included in Table 5, corresponds to the quality of measurements of this transition. For further analysis, we adopt the most reliable values of T_e, that is we take a mean value of T_e([O III]) and T_e([S III]) to represent region B1 and T_e([N II]) in regions A1 and A2. In region B2 we have no reliable estimate of T_e. Since the spectrum of this region shows a similar degree of excitation as that of region B1, we adopted for region B2 the same T_e as for region B1, i.e. T_e=15000 K. Region C, where we cannot reliably estimate T_e, exhibits similar excitation as regions A1 and A2. Therefore, we adopted T_e=10000 K for region C.

The second part of Table 5 presents our estimates of N_e. For further analysis of regions A1, A2, and C, we adopted mean values of N_e derived from the line ratios of [O II] and [S II]. In the case of regions B1 and B2, no measurements of line ratios sensitive to N_e are available. Instead, we estimated N_e from comparing the surface brightness of Hβ in regions A and B. Note that the emissivity in Hβ is proportional to N_e^2. As can be seen in Fig. 4, Hβ is slightly stronger in region B1 than in region A1. Therefore, we adopted N_e=600 cm^{-3} for region B1. Similarly, comparing the Hβ flux in region B2 to that in A2 (see Fig. 5), we adopted N_e=200 cm^{-3} for B2. Note that the ion abundances are rather insensitive to the actual value of N_e in the range relevant for our spectra, i.e., for $N_e \lesssim 10^4$ cm^{-3} (see also below).

As can be seen in Table 5, the [N II] ratio in region B1 yields T_e=26500 K. This is much higher than the temperature

Table 3. The same as Table 1 but for component C in spectrum 3.

λ_0 (nm)	Ion	Flux (10^{-16} erg cm^{-2} s^{-1})	Relative flux (Hβ=100)	V_r (km s^{-1})	FWHM (km s^{-1})	Note
372.60	[O II]	0.0292	81.8	–279	85	b
372.88	[O II]	0.0310	86.8	–273	97	b
434.05	H I	0.0131	36.7	–278	82	b
486.13	H I	0.0357	100.0	–282	82	a
495.89	[O III]	0.0082	23.0	–274	104	c
500.68	[O III]	0.0241	67.5	–276	99	b
519.79	[N I]	0.0136	38.1	–286	68	b
520.03	[N I]	0.0175	49.0	–275	73	b
575.46	[N II]	0.0070	19.6	–269	57	d
587.56	He I	0.0069	19.3	–286	52	d
630.03	[O I]	0.0505	141.5	–298	85	b
636.38	[O I]	0.0177	49.6	–288	66	c
654.80	[N II]	0.1248	349.6	–288	89	a
656.28	H I	0.2778	778.2	–292	89	a
658.34	[N II]	0.4120	1154.1	–290	87	a
671.64	[S II]	0.1080	302.5	–289	78	a
673.08	[S II]	0.0978	273.9	–292	80	a
715.52	[Fe II]	0.0115	32.2	–295	66	c
729.15	[Ca II]	0.0442	123.8	–295	64	c
861.70	[Fe II]	0.0205	57.4	–285	78	c
906.86	[S III]	0.0064	17.9	–270	71	d
953.06	[S III]	0.0250	70.0	–266	97	c
982.41	[C I]	0.0268	75.1	–270	80	c
985.03	[C I]	0.0952	266.7	–291	82	b

Notes. The first two columns identify the lines. The four subsequent columns present results of Gaussian fits to component C. Notation as in Table 2.

decades). Thus, the statistical equilibrium can be safely adopted when calculating the populations of low-lying levels of atoms and ions.

[4] www.astronomy.ohio-state.edu/~pradhan/atomic.html

Table 4. Intensities of the emission lines corrected for the reddening. The values of the adopted extinction, $C(\mathrm{H}\beta)$, and reddening, E_{B-V}, are given for the individual regions in the second and third row, respectively.

region:		A1		A2		B1		B2		C	
$C(\mathrm{H}\beta)$:		1.35		1.40		1.40		1.35		1.32	
E_{B-V}:		0.90		0.93		0.93		0.90		0.88	
Ion	λ (nm)	$I_\lambda/I_{\mathrm{H}\beta} \cdot 100$ and its uncertainity flag									
H I	486.13	100.0	a	100.0	a	100.0	a	100.0	a	100.0	a
H I	397.01	12.3	c			13.0	c				
H I	410.17	27.3	b	30.6	b	26.8	b	18.2	d		
H I	434.05	51.3	b	53.8	b	49.9	b	49.7	b	56.8	b
H I	656.28	287.0	a	286.4	a	281.8	a	287.2	a	282.2	a
H I	901.49	2.0	c	2.0	c	1.6	c				
H I	922.90	2.6	c	2.4	c	2.5	c				
H I	954.60	2.8	c			2.7	c				
H I	1004.98	6.0	c			5.7	c				
He I	388.86	24.0	c	25.0	b	25.0	c	53.0	c		
He I	447.15	9.6	c	12.3	c	12.3	c				
He I	501.57	7.6	c			8.4	c				
He I	587.56	31.4	a	30.9	a	40.8	a	53.2	b	9.9	d
He I	667.82	9.8	b	9.4	b	9.7	b	14.4	c		
He I	706.52	5.8	b	5.9	b	23.4	a	33.9	b		
He II	468.57	6.9	c			7.2	c				
[C I]	872.71			1.5	c						
[C I]	982.41	12.7	b	19.8	b					10.7	c
[C I]	985.03	32.2	a	56.0	a					38.0	b
[N I]	519.79	54.3	b	71.3	a					29.7	b
[N I]	520.03	65.8	b	77.3	a					38.2	b
[N II]	575.46	16.6	b	11.5	c	17.4	b			10.7	d
[N II]	654.80	383.2	a	269.0	a	91.4	b	153.1	b	127.6	a
[N II]	658.34	1184.9	a	842.4	a	273.5	b	318.3	a	414.7	a
[O I]	630.03	48.2	b	42.2	a					58.0	b
[O I]	636.38	17.0	b	14.7	b					19.7	c
[O II]	372.60	145.5	a	112.4	a					232.5	b
[O II]	372.88	133.5	a	114.3	a					246.1	b
[O III]	436.32					17.4	b	18.4	d		
[O III]	495.89			2.5	d	311.4	a	533.0	a	21.3	c
[O III]	500.68			7.1	c	929.8	a	1583.7	a	60.4	b
[Ne III]	386.88			18.8	c	306.0	a	535.1	a		
[Ne III]	396.75			5.7	d	69.5	a	141.3	b		
[S II]	671.64	136.4	a	130.0	a					102.7	a
[S II]	673.08	131.6	a	120.0	a					92.4	a
[S III]	631.21					4.8	b				
[S III]	906.86	3.0	c	1.7	d	39.4	a	45.2	a	3.0	d
[S III]	953.06	7.1	b	5.1	c	100.7	a	136.0	a	10.6	c
[Ar III]	713.58					30.1	a	41.4	a		
[Fe II]	715.52	10.1	b	4.9	b					9.2	c
[Fe II]	717.20	1.6	c								
[Fe II]	745.26	3.2	c								
[Fe II]	861.70	20.4	b	10.2	b					10.6	c
[Fe II]	889.19			4.1	b						
[Fe II]	905.20	5.5	b								
[Fe II]	922.66	4.2	b	1.2	c						
[Ni II]	737.78	13.1	b	5.7	b						
[Ca II]	729.15	27.6	b	18.6	b					33.6	c
[Ca II]	732.39	29.0	b	12.7	b						

Notes. The intensities are expressed relative to Hβ and scaled by 100. They are associated by quality flags a–d which are consistent with the notation in Tables 1–3.

derived from the line ratio of [O III] or [S III]. The discrepancy may suggest that the density in region B1 is actually higher than the adopted value of 600 cm^{-3}. Indeed, T_e derived from the [N II] ratio is more sensitive to N_e than in cases of [O III] and [S III], especially at higher N_e. Our calculations show that at N_e=4 × 10^4 cm^{-3} the three line ratios would indicate similar temperatures of about 13800 K. At this high density, however, the emissivity of Hβ in region B1 would be almost 10^4 times higher than that in region A1, whereas the measured fluxes of Hβ in regions A1 and B1 are comparable (Table 1). This implies that the volume occupied by nebular matter in region B1 is ∼ 10^4 times smaller than in region A1. Yet, the extent along the slit and in the range of radial velocities of component B are similar to that of component A (Fig. 3). The only way to reconcile these contradictions is to propose a two-phase structure of region B1. Namely that the bulk of the emission comes from a thin

Table 5. Physical conditions, T_e and N_e, and abundances derived for the individual regions.

region	A1		A2		B1		B2		C	
	T_e (K)									
[O III]					14800	b	12200	d		
[S III]					15000	b				
[N II]	10100	b	10100	c	26500	b			13700	d
[C I]			6310	c						
adopted	**10100**		**10100**		**14900**		**15000**		**10000**	
	N_e (cm^{-3})									
[O II]	585	a	417	a					357	b
[S II]	503	a	414	a					364	a
[N I]	188	b	323	a					129	b
adopted	**544**		**415**		**600**		**200**		**360**	
	ionic abundances									
N^+/H^+	2.17E–4	a	1.57E–4	a	2.12E–5	b	2.69E–5	a	7.79E–5	a
O^+/H^+	1.08E–4	a	8.83E–5	a					1.90E–4	b
O^{++}/H^+			2.39E–6	c	9.89E–5	a	1.66E–4	a	2.10E–5	b
Ne^{++}/H^+			1.49E–5	d	5.94E–5	a	1.05E–4	b		
S^+/H^+	5.87E–6	a	5.42E–6	a					4.26E–6	a
S^{++}/H^+	3.53E–7	b	2.44E–7	c	2.55E–6	a	3.27E–6	a	4.90E–7	c
Ar^{++}/H^+					1.21E–6	a	1.64E–6	a		
	elemental abundances									
He/H	0.229		0.228		0.259		0.391			
N/H	2.17E–4		1.61E–4						8.65E–5	
O/H	1.08E–4		9.07E–5		9.89E–5		1.66E–4		2.11E–4	
Ne/H					5.94E–5		1.05E–4			
S/H	6.22E–6		5.67E–6		2.55E–6		3.27E–6		4.75E–6	
Ar/H					1.21E–6		1.64E–6			

Notes. The letters next to the physical quantities indicate the quality of the original flux measurements of the relevant lines: a, flux accurate to within 10%; b, error between 10 and 30%; c, error greater than 30%; d, line marginally detected.

($N_e \approx 600\,\mathrm{cm}^3$) medium of high excitation (doubly ionized O, Ne, S, and Ar), in which there are small but dense inclusions of low ionization that give rise to the [N II] emission.

Having determined T_e and N_e, we calculated the emissivity of Hβ and of the forbidden lines, see e.g. Ch. 5.11 in Osterbrock & Ferland (2006). Comparing the emissivity in a given line normalized to Hβ with the corresponding measured intensities, we obtained the ion abundances relative to ionized hydrogen. The results are given in Table 5.

We next discuss uncertainties in the derived abundances. The accuracy of ionic abundances depend mainly on the precision of measurements of the line intensities. When calculating the ionic abundances, we used the strongest lines of a given ion, i.e. the lines whose fluxes were most accurately measured. For example, the abundance of O^{++} was obtained from the sum of the flux of [O III] 495.9 and 500.7. Thus, at this stage, the derived values are accurate to a few percent. However, the line emissivities depend not only on the ion abundances but also on the electron density and temperature, N_e and T_e. The derivation of these parameters were often based on weaker lines, and this can be a source of larger uncertainties in the final abundances.

N_e was mainly estimated from the line ratios of [O II] and [S II]. These intensities were usually quite precisely measured (quality flag a in Tables 1–3). Our calculations show that a 10% uncertainty in these line ratios results in a 30–40% uncertainty in N_e. Although, the error is quite large, it has a negligible effect on the final ionic abundances, as the resulting uncertainty in the abundances never exceeds 4%.

T_e was calculated from the line ratios of [N II], [O III], and [S III]. These ratios involve the emission from the ($^1S - ^1D$) transition, which is usually quite faint (quality flag b, at best). Calculations show that a 20% uncertainty in the involved line ratios results in a 7 – 10% uncertainty in T_e. However, this small error in T_e causes much larger errors in the abundances since the line emissivities depend exponentially on T_e. Because of this exponential dependence the error of ionic abundances also depends on the excitation energy of the transition, in other words, on the wavelength of the line used to derive the abundance. The shorter the wavelength, the larger the error. In our case, the final uncertainties in the ionic abundances range from 16% for S^{++}, ~20% for S^+, N^+ and Ar^{++}, 28% for O^{++}, up to ~35% for Ne^{++} and O^+.

Not every ion of a given element is observable in the wavelength range covered by our observations. This has to be taken into account when deriving the abundances of the elements. The standard way is to apply the so-called ionization correction factors, usually calculated from steady-state photoionization models (e.g. Delgado-Inglada et al. 2014). However, it would be somewhat risky in our case, as it is not clear what the primary ionization mechanism is operating in the nebular regions in CK Vul. In Sect. 6.1, we argue that these are shocks rather than photoionization by the central star. In the case of shocks the optical emission lines are mainly produced in ambient matter photoionized by radiation emitted in the hot post-shock region and/or in matter recombining from the hot, highly ionized post-shock conditions. Finally, at the observed densities ($N_e \approx 500\,\mathrm{cm}^{-3}$) the recombination time is long (~250 years for H^+). Therefore we can also deal with matter that was ionized in the past and is now recombining. The state of the latter can be far from ionization equilibrium conditions. Therefore, we follow a more general reasoning that allows us to get reliable estimates of the total elemental abundances, independent of the actual ionization mechanism and history.

The low flux of the He II 468.6 line assures that the abundance of He^{++} is negligible in all the investigated regions. Indeed, our measurements of this line (see Table 4) yield a ratio

$He^{++}/H^+ \lesssim 0.005$. We thus neglect the He II 468.6 line while determining the He abundance. Consequently, the abundance of helium was derived from the intensities of the He I lines only. We used He I emissivities of Benjamin et al. (1999). Their formulas, besides the recombination cascades, take into account collisional effects. The lines He I 388.9 and 706.5 can be subject to radiative-transfer effects (see e.g. Ch. 4.6 in Osterbrock & Ferland 2006), so we excluded them from our abundance calculations. The final He abundance was obtained as a weighted mean of values derived from each individual line. The weights were assigned according to the precision of the original flux measurement. The results are given in Table 5. Uncertainties of the listed He abundances do not exceed 15%.

The negligible abundance of He^{++} allows us to assume that all ions with an ionization potential ≥54.4 eV are practically absent. This concerns the following (or higher) ions of interest: N^{4+}, O^{3+}, Ne^{3+}, S^{5+}, and Ar^{4+}. All these ions have recombination coefficients much larger than that of He^{++} and very fast rates of charge transfer with H^0 (Kingdon & Ferland 1996). Therefore if the ionization processes cannot maintain a substantial abundance of He^{++}, they have even more difficulties with making the above ions abundant.

Thus, in the case of oxygen, all the presumably abundant ions, i.e. O^+ and O^{++}, are observed and we assume

$$O/H = (O^+/H^+) + (O^{++}/H^+).$$

In the case of nitrogen, only N^+ is observed, while N^{++} and N^{3+} can be potentially abundant. In component B, the latter ions are probably dominant. Therefore we cannot reliably estimate the N abundance in region B. In component A (and C), the [N II] lines are very strong. This suggests that N^+ is the dominant ion of N. This conviction is strengthened by the weakness of [O III] lines and consequently the very low abundance of O^{++} in component A. We adopted the following formula

$$N/H = (N^+/H^+)(O^+/H^+)/(O/H)$$

when determining the N abundance. This is a standard ionization correction formula used in the case of photoionized nebulae. In our case of component A, it practically assumes that the N abundance is equal to the observed abundance of N^+. If N^{++} is substantially abundant, then we underestimate the N abundance.

Sulfur is the second element, after oxygen, whose two ionization states, i.e. S^+ and S^{++}, are observed in CK Vul. However, contrary to O, we cannot simply assume that these are the only ions of S that are abundant, as the presence of S^{3+}, or even S^{4+}, cannot be excluded. This is particularly relevant for component B where the [S III] lines are strong and those of [S II] are not observed. Nevertheless, we adopt

$$S/H = (S^+/H^+) + (S^{++}/H^+)$$

as nothing better can be done at this time. We expect this is a good approximation in component A (and C), as S^{++} is there at least an order of magnitude less abundant than S^+ and therefore the abundances of S^{3+} and S^{4+} should be negligible. The latter is not expected in component B and thus our procedure yields an underestimated abundance of S in region B. This systematic error has a confirmation in our final results for all the regions in Table 5 where S/H in component B is systematically lower than that in component A and C. Such discrepancy is not expected if the relative elemental abundances are constant throughout the small part of the nebula probed with the X-shooter slit.

Neon and argon are observed only in component B and only in the form of doubly ionized species. In the case of neon, Ne^{++} is most probably the dominant ion in component B. Ne^+ should be negligible, because O^+ is not observed. Admittedly, Ne^+ has a higher ionization potential than O^+ but a very low rate of charge transfer between Ne^{++} and H^0, compared to that between O^{++} and H^0 (Kingdon & Ferland 1996), should compensate for the effect caused by the difference in ionization potentials. Therefore, we simply assume

$$Ne/H = Ne^{++}/H^+.$$

In the case of argon, Ar^{3+} cannot be excluded as an important ion in component B. Therefore, a determination of Ar abundance solely from the measured abundance of Ar^{++}, i.e.

$$Ar/H = Ar^{++}/H^+,$$

leads to an underestimated abundance of this element.

With the elemental abundances obtained for individual regions in Table 5, we derived the mean abundances representing all the regions. When averaging, the results from regions B2 and C were weighted twice lower than those from the other regions. The spectra from these two regions are significantly fainter and, consequently, the measurements of line intensities were less precise than those in the other regions. As a result, we were unable to derive reliable estimates of the electron temperature, which introduced an additional uncertainty in the abundances for these two regions. When calculating the mean abundance of sulfur, we omitted the results obtained for component B, because they probably underestimate the S/H value (see above). The upper part of Table 6 lists the mean number abundances and their estimated errors. The bottom part of Table 6 presents the same abundances but in mass fractions. For comparison, we also listed the abundances of the Sun from Asplund et al. (2009).

Table 6. Mean elemental abundances of CK Vul compared to solar ones.

relative abundances by number:			
	CK Vul	error	Sun
He/H	0.260	±21%	0.085
N/H	1.69E–4	±29%	6.76E–5
O/H	1.22E–4	±34%	4.90E–4
Ne/H	7.45E–5	±29%	8.50E–5
S/H	5.70E–6	± 9%	1.32E–5
Ar/H	1.35E–6	±15%	2.50E–6
abundances by mass:			
	CK Vul	error	Sun
H	0.488	±18%	0.740
He	0.509	±28%	0.252
N	1.15E–3	±35%	7.01E–4
O	9.50E–4	±40%	5.80E–3
Ne	7.27E–4	±35%	1.26E–3
S	8.91E–5	±16%	3.13E–4
Ar	2.64E–5	±21%	7.40E–5

6. Discussion

6.1. The excitation mechanism of the nebula

There are two possible mechanisms producing nebular line emission: direct ionization by stellar radiation and excitation by shock fronts. It is not straightforward to distinguish between these two mechanisms from observations of line intensities alone. This is because in the case of shocks, the nebular lines, especially in the optical, are excited mostly through ionization by radiation generated in the shock. Both mechanisms are essentially incarnations of photoionization. In the case of CK Vul,

there are however several arguments favoring shocks instead of photoionization by a hot central star.

First, we do observe gas moving at high velocities. As can be seen in Fig. 3, the observed radial velocities range from ∼–300 to ∼+350 km s^{-1}. The de-projected gas velocities are probably much higher. Indeed, the large-scale hourglass optical nebula studied by Hajduk et al. (2013) appears to have a large inclination of about 65° at which the gas moves mainly perpendicular to the line of sight and the tips of that nebula are estimated to move as fast as 900 km s^{-1}. Dissipation in shocks with velocities of a few hundreds of km s^{-1} can result in gas temperatures above 10^6 K and produce intense ultraviolet and X-ray radiation capable of photoionizing large volumes of the surrounding medium (Dopita & Sutherland 1996).

Second, the emission lines of neutral CNO elements (that is, [C I], [N I], and [O I]) and singly ionized metals ([Fe II], [Ni II], and [Ca II]) are particularly strong in the spectrum of CK Vul. This is generally considered as a signature of shock-excited emission regions (e.g. Dopita & Sutherland 1995). Shocks, contrary to photoionizantion by a star, produce extended recombination regions of a low ionization degree, where hydrogen and elements having similar ionization potential as hydrogen – such as N and O – remain largely neutral, while elements of low-ionization potentials – including, Fe, Ni, and Ca – are predominantly singly ionized (e.g. Dopita & Sutherland 1996).

Third, we do not observe any significant variation of the ionization and excitation conditions with the radial distance from the position of the presumable central object. Regions A2 and B2 are significantly farther away from the location of the central star than regions A1 and B1, respectively. Yet, comparing regions A1 with A2 and B1 with B2, their spectra (Table 4) as well as the ionization degrees and temperatures (Table 5) are very similar. We do, however, observe that the regions at the same (projected) distance from the central star but at different radial velocities, i.e. A1 and B1 or A2 and B2, have drastically different spectra and ionization states. In the case of photoionization by a star, this would imply that the star emits drastically different spectra in different directions, which is unlikely. The differences between components A and B can, however, be easily understood, if they are powered by shocks. The lower ionization and excitation degree of component A may imply that the matter at negative radial velocities was shock-excited some time before the matter of component B (at positive radial velocities). Component A had thus more time to recombine and cool off than component B. We note that at the derived electron densities (∼500 cm^{-3}) the recombination time of ionized hydrogen is ∼250 years. Ions, like O^{++} and Ne^{++}, recombine much faster than H^+.

Another way of explaining the differences between component A and B in terms of shocks is to assume that component B was excited by a stronger shock than component A. In the case of low-velocity shocks ($v_s \lesssim 150$ km s^{-1}), the Balmer decrement is steeper than that of the recombination case B (Dopita & Sutherland 2017). This is because collisional excitation of Hα is important in an extended region of partial ionization generated by slow shocks. This seems to be observed in CK Vul, particularly in components A and C. When constraining the excitation conditions in Sect. 4, we paid attention to reproduce the case B ratio of Hα to Hβ as this ratio is best determined observationally and is most sensitive to extinction. The results in Table 4 were obtained under this assumption. However, for all components in this table, the Hγ relative line intensity is greater than the value of ∼47 corresponding to pure recombination. The excess ranges from ∼6% in component B to ∼20% in component C. Formally, its magnitude is within the measurement errors but it may be significant because it appears in all the regions and is correlated with the excitation and ionization state of the components.

We therefore made an exercise and derived the extinction value from Hγ/Hβ. This ratio is supposed to be much less affected by collisional excitation than Hα/Hβ. We obtained C(Hβ) equal to 0.75 for component C, 1.00–1.08 for component A, and 1.22–1.25 for component B. These values can be compared to those in Table 4. After correcting the observations using these new values of extinction, we obtained the relative Hα intensity ranging from ∼317 for component B, 353–389 for component A, and 437 for component C. According to Dopita & Sutherland (2017), these values would correspond to shock velocities of ∼35 km s^{-1} for component C, ∼60 km s^{-1} for component A, and ∼100 km s^{-1} for component B. A detailed comparison of the models of Dopita & Sutherland (2017) with our spectra is beyond the scope of the present paper. In fact, it would not be straightforward because of significant differences in the elemental abundances. Moreover, our measurements probe only a narrow cut through the nebular region of CK Vul and probably encompass only a part of a shock-excited region. We are unable to state which particular parts of the shock-excited region were observed (e.g. a precursor or postshock flow as in Sutherland & Dopita) whereas such a distinction would be crucial for comparing our line intensities with the models. Nevertheless, the above estimates on v_s increase with the increasing excitation of the observed spectra, as expected from the models. For instance, the models predict significant emission in the [O III] lines only for $v_s \gtrsim 80$ km s^{-1}; that is consistent with the observation of [O III] in component B only.

It should, however, be emphasized that the above arguments in favor of shock excitation are not fully conclusive. Any information on the effective temperature or spectral type of the central object would be more decisive in this matter. Unfortunately nothing of this kind can be derived from the observational data currently available for CK Vul.

6.2. The abundances and nature of CK Vul

The elemental abundances in the nebular region of CK Vul presented in Table 6 are the primary result of this study. They are based on the spectra corrected for the extinction derived in a standard way, i.e. assuming that the true Balmer decrement is that of the recombination case B. In Sect. 6.1, we discussed the possibility of excitation by slow shocks, which produce the Hα/Hβ ratio well above the classical recombination value. Shock excitation results in extinction values that are significantly lower than those derived assuming the pure recombination decrement. In order to derive abundances in the framework of slow shocks, the line intensities should be recalculated with the relevant extinction.

We therefore repeated the abundance determination using the extinction values derived from the observed ratio of Hγ/Hβ (see Sect. 6.1). For component B, the resultant abundances are close to those in Table 5. Larger differences are noticeable for components A and C. The new abundances are more consistent with each other than those in Table 5. As a result, the uncertainties of the final averaged abundances, presented in Table 7, are smaller than those in Table 6.

In Fig. 6, we compare the elemental abundances derived for classical case B (from Table 6) and in the presence of shocks (from Table 7). The differences are insignificant. Note, however, that the N/O ratio increases from ∼1.2 in Table 6 (extinction derived from Hα/Hβ) to ∼1.9 in Table 7 (extinction from Hγ/Hβ).

Table 7. Mean elemental abundances of CK Vul derived from the spectra corrected for extinction using the observed Hγ/Hβ (see Sect. 6.1).

abundances by mass:		
	CK Vul	error
H	0.458	±17%
He	0.538	±24%
N	1.59E–3	±28%
O	8.30E–4	±30%
Ne	6.70E–4	±28%
S	1.26E–4	±10%
Ar	2.98E–5	±15%

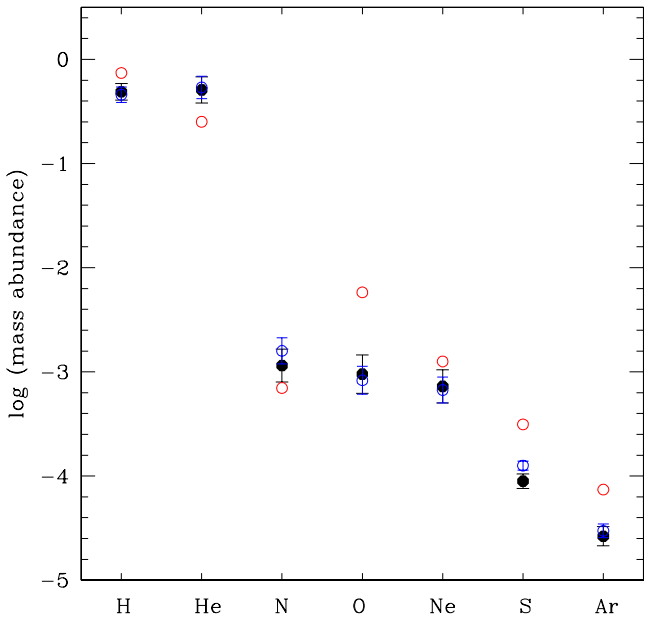

Fig. 6. Elemental mass abundances in CK Vul. Black dots: abundances from Table 6. Blue circles: abundances obtained from the spectra corrected for extinction using the observed Hγ/Hβ ratio, as explained in Sect. 6.1. Red circles: abundances in the sun.

In any case, the abundances we obtained for CK Vul are significantly different from the solar values. Helium is overabundant by a factor of two, which implies that ∼25% of hydrogen in the observed matter has been converted to helium. As a result, the mass abundance of helium is comparable to that of hydrogen. Unfortunately, we were not able to derive the carbon abundance, but the obtained abundances of nitrogen and oxygen show that a significant part of the CNO elements were converted to nitrogen. This is apparent when comparing the N/O ratio, which is ∼1.2–1.9 in CK Vul, with the much lower solar value of 0.12. The latter result confirms the suggestion of Kamiński et al. (2015a, 2017), based on submm spectral analysis, that the remnant of CK Vul is rich in nitrogen. Overall, the current study strongly reinforces the conclusion drawn from the isotopic study of molecular lines that the remnant's material has been processed in H-burning in CNO cycles. Possible scenarios for this processing were discussed in Kamiński et al. (2017) (see also Kamiński et al. 2018b).

Table 6 also shows that neon, sulfur, and argon are underabundant in CK Vul compared to the Sun. The abundances of these elements are not affected in the CNO cycles. As can also be seen in Table 6, the summary abundance of oxygen and nitrogen in CK Vul is three times lower than in the Sun. The CNO cycles do not alter the summary abundance of the CNO elements but mainly convert carbon and oxygen to nitrogen. Therefore, we may conclude that elements heavier than helium were less abundant in the matter from which the progenitor of CK Vul was formed than in the Sun. Using the ζ-scaling of elemental abundances with metallicity of Nicholls et al. (2017)[5], for Ne, S and Ar we find [Fe/H]=–0.53±0.07. This low-metallicity chemical composition strongly suggests that the progenitor of CK Vul was older than the Sun.

6.3. Extinction

The observed spectrum of CK Vul is significantly reddened. This is mainly due to interstellar extinction but a contribution from internal dust in CK Vul is not excluded. The observed nebular region ("jet") is situated inside the northern lobe seen in the submillimeter dust-emission (Kamiński et al. 2018b; Eyres et al. 2018). Therefore it is likely that part of the observed reddening is due to local dust situated *outside* the observed nebular region but crossed by the line of sight. High interstellar extinction towards CK Vul is expected based on its low Galactic latitude of 1° and on observations of interstellar CO lines (Kamiński et al. 2017).

The values of extinction listed in Table 4 are practically the same for all the investigated regions, i.e. $C(\mathrm{H}\beta) \simeq 1.36$ ($E_{B-V} \simeq 0.91$). This could suggest that there is no significant reddening inside the nebular region itself. However, adopting the hypothesis of slow shocks and determining the extinction from the observed Hγ/Hβ ratio instead of Hα/Hβ (see Sect. 6.1), we derived extinction values which are lower and significantly different for different regions: that is, $C(\mathrm{H}\beta) \simeq 0.75$ for component C, ∼1.04 for component A, and ∼1.24 for component B. We note that the derived C values correlate with the mean radial velocities of the regions (see Sect. 4), i.e. –285 km s^{-1} for component C, ∼–130 km s^{-1} for component A, and ∼+75 km s^{-1} for component B. The regions of negative radial velocities are expected to be closer to us than the one moving with the positive velocity. Therefore, in this case, we would have to conclude that the extinction within the nebular region is significant and that the extinction obtained for component C, $C(\mathrm{H}\beta) \simeq 0.75$, is an upper limit to the interstellar extinction.

7. Summary

We obtained an optical spectrum of the brightest nebular region of CK Vul, a remnant of an ancient stellar explosions observed in 1670–72. The spectrum was recorded with the X-shooter spectrograph at the VLT and reveals a plethora of ionic emission lines typical for spectra of planetary nebulae. An analysis of the spectrum indicates the presence of several spatio-kinematical regions located ∼1″.3–8″.5 from the presumed position of the star. From the measured line intensities, we estimated the electron temperatures, typically of 10–15 kK, and densities of 200–600 cm^{-3} prevailing in the individual regions. This allows us to derive abundances of the ions emitting the observed lines and also the abundances of several key elements, including H, He, O, and N. Despite the different excitation conditions within the nebula, the elemental abundances derived for individual regions are very similar. We found that helium is overabundant by a factor of two compared to the Sun. Also, nitrogen is overabundant. This is particularly well seen in the N/O ratio which is ten times higher than the solar one. These findings clearly show that the matter

[5] see https://miocene.anu.edu.au/mappings/abund/

in the remnant of CK Vul has been processed in the CNO cycles of H-burning. Other elements, such as neon, sulfur, and argon, are underabundant compared to the Sun. We have found that the overall abundance of the CNO elements in CK Vul is also lower than in matter of solar (cosmic) composition. Clearly, the progenitor of CK Vul was an old system, much older than the Sun. The derived abundances together with other recent observational results will be discussed in a separate paper devoted entirely to revealing the nature of CK Vul and its progenitor. Finally, we argue that the nebular regions in CK Vul are excited by shocks rather than being directly photoionized by a central star.

Acknowledgements. We thank our referee and editor, S. Shore, for comments on the manuscript. We are grateful to M. Hajduk for making available to us his processed Gemini image of CK Vul. Based on observations collected at the European Organisation for Astronomical Research in the Southern Hemisphere under ESO programme 099.D-0010(A). R.T. acknowledges a support from grant 2017/27/B/ST9/01128 financed by the Polish National Science Centre.

References

Asplund, M., Grevesse, N., Sauval, A. J., et al. 2009, ARA&A, 47, 481
Benjamin, R. A., Skillman, E. D., & Smits, D. P. 1999, ApJ, 514, 307
Bertin, E., Mellier, Y., Radovich, M., et al. 2002, Astronomical Data Analysis Software and Systems XI, 281, 228
Delgado-Inglada, G., Morisset, C., & Stasińska, G. 2014, MNRAS, 440, 536
Dopita, M. A., & Sutherland, R. S. 1995, ApJ, 455, 468
Dopita, M. A., & Sutherland, R. S. 1996, ApJS, 102, 161
Dopita, M. A., & Sutherland, R. S. 2017, ApJS, 229, 35
Draine, B. T. 2003, ARA&A, 41, 241
Evans, A., van Loon, J. T., Zijlstra, A. A., et al. 2002, MNRAS, 332, L35
Evans, A., Gehrz, R. D., Woodward, C. E., et al. 2016, MNRAS, 457, 2871
Eyres, S. P. S., Evans, A., Zijlstra, A., et al. 2018, MNRAS, 481, 4931
Górny, S. K. 2014, A&A, 570, A26.
Hajduk, M., Zijlstra, A. A., van Hoof, P. A. M., et al. 2007, MNRAS, 378, 1298
Hajduk, M., van Hoof, P. A. M., & Zijlstra, A. A. 2013, MNRAS, 432, 167
Hevelius, J. 1671, Philosophical Transactions of the Royal Society of London Series I, 6, 2197
Kamiński, T., Menten, K. M., Tylenda, R., et al. 2015, Nature, 520, 322
Kamiński, T., Menten, K. M., Tylenda, R., et al. 2017, A&A, 607, A78
Kamiński, T., Steffen, W., Tylenda, R., et al. 2018a, A&A, 617, A129
Kamiński, T., Tylenda, R., Menten, K. M., et al. 2018b, Nature Astronomy, 2, 778
Kausch, W., Noll, S., Smette, A., et al. 2015, A&A, 576, A78
Kato, T. 2003, A&A, 399, 695
Kingdon, J. B. & Ferland, G. J. 1996, ApJS, 106, 205
Mason, E., Diaz, M., Williams, R. E., et al. 2010, A&A, 516, A108
Modigliani, A., Goldoni, P., Royer, F., et al. 2010, Proc. SPIE, 7737, 773728
Munari, U., Henden, A., Kiyota, S., et al. 2002, A&A, 389, L51.
Nicholls, D. C., Sutherland, R. S., Dopita, M. A., et al. 2017, MNRAS, 466, 4403
Osterbrock, D. E., & Ferland, G. J. 2006, Astrophysics of Gaseous Nebulae and Active Galactic Nuclei, University Science Books
Pradhan, A. & Peng, J. 1995, Space Telescope Science Institute Symposium Series No. 8, Eds.: R.E. Williams and M. Livio, Cambridge University Press
Shara, M. M., & Moffat, A. F. J. 1982, ApJ, 258, L41
Shara, M. M., Moffat, A. F. J., & Webbink, R. F. 1985, ApJ, 294, 271
Smette, A., Sana, H., Noll, S., et al. 2015, A&A, 576, A77
Soker, N., & Tylenda, R. 2003, ApJ, 582, L105
Tylenda, R., & Soker, N. 2006, A&A, 451, 223
Tylenda, R., Hajduk, M., Kamiński, T., et al. 2011, A&A, 528, A114
Tylenda, R., Kamiński, T., Udalski, A., et al. 2013, A&A, 555, A16
Udalski, A. 2003, Acta Astron., 53, 291
Vernet, J., Dekker, H., D'Odorico, S., et al. 2011, A&A, 536, A105